



Measurement and Estimation of Weld Pool Surface Depth and Weld Penetration in Pulsed Gas Metal Arc Welding

A relationship between a change in arc voltage at peak current and depth of joint penetration was established

BY Z. WANG, Y. M. ZHANG, AND L. WU

ABSTRACT

The weld pool surface may contain sufficient information to determine weld penetration. In this study, a high-speed camera-based vision system was used to image the weld pool surface during gas metal arc welding (GMAW). To calculate the depth of the weld pool surface from the acquired image, a calibration procedure is proposed to determine the parameters in the calculation equation. Welding parameters were designed to conduct a series of pulsed GMAW

(GMAW-P) experiments. Modeling using experimental data shows that the change of the weld pool surface depth during the peak current period can predict the depth of the weld penetration with adequate accuracy. However, a direct application of this result is complicated by the need for a vision system. To find a method that can be used to monitor the weld penetration using signals that are easily measurable in manufacturing facilities, a possible relationship between a change in weld pool surface depth and a change in arc voltage was an-

alyzed. The analysis suggested that the change in arc voltage during the peak current period may reflect accurately the change in weld pool surface depth during the peak current period. As a result, it is proposed that the depth of the weld penetration be determined from the change in arc voltage during the peak current period. The modeling result shows that the change in arc voltage during peak current can indeed provide an accurate prediction for the depth of the weld penetration during GMAW-P.

Introduction

Gas metal arc welding (GMAW) can be considered the most widely used arc welding process, preferred for its versatility, speed, and easy application in robotic automation. Pulsed GMAW (GMAW-P) is used to achieve a controlled metal transfer process over wide ranges of heat and mass input levels (Refs. 1, 2). It uses a low amperage to maintain the arc and a peak amperage to melt the welding wire and detach the resultant droplet. As a result, the desired spray transfer can be achieved at low average currents (Refs. 3, 4).

Weld penetration plays a fundamental role in determining the mechanical strength of welds, and thus, its control is

critical. This study concerns partial penetration applications where the base metal is not fully melted through its entire thickness. For partial penetration applications, how deep the base metal is melted is referred to as the depth of weld penetration. This depth is often used as the measurement of the weld penetration. It is apparent that the depth of weld penetration is not directly visible. Many methods have been introduced to estimate it based on indirect measurements such as geometrical parameters of the weld pool (Ref. 5), temperature field (Ref. 6), oscillation frequency (Refs. 7, 8), and arc voltage (Ref.

9). To obtain indirect measurements, various techniques such as vision (Refs. 5, 10), ultrasonic (Ref. 11), acoustic emission (Ref. 12), and thermal (Ref. 6) have been used. However, most of those efforts focused on gas tungsten arc welding (GTAW). The GTAW process is less complex and much more stable in comparison with GMAW, which is the concern in this study. The GMAW process uses a consumable wire as an electrode to improve the productivity, and the resultant metal transfer of the melted wire complicates the process. Because of the metal transfer, the droplets impact the liquid weld pool periodically and cause the weld pool to fluctuate. For the pulsed GMAW studied in this paper, the arc pressure also changes periodically, resulting in significant fluctuation in the weld pool surface. The resultant complexity added additional difficulties to obtain indirect measurements needed to estimate the weld penetration.

Among the possible indirect measurements, the weld pool surface appears to be the most promising one with sufficient information to estimate the weld penetration. This is because many skilled welders

Z. WANG and Y. M. ZHANG (ymzhang@engr.uky.edu) are with the State Key Laboratory of Advanced Welding Production Technology, Harbin Institute of Technology, Harbin, China; and Center for Manufacturing and Department of Electrical and Computer Engineering, University of Kentucky, Lexington, Ky; L. WU is with the State Key Laboratory of Advanced Welding Production Technology, Harbin Institute of Technology, Harbin, China.

KEYWORDS

Weld Penetration
Weld Pool Surface
Monitoring
Modeling
GMAW-P
Machine Vision

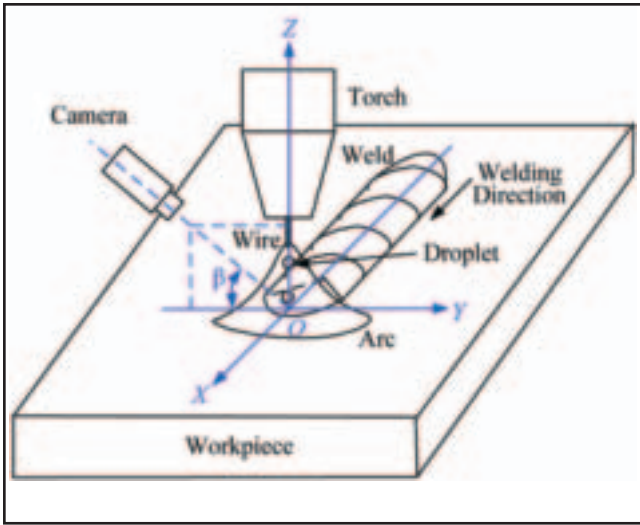


Fig. 1 — Schematic diagram for SD measurement.

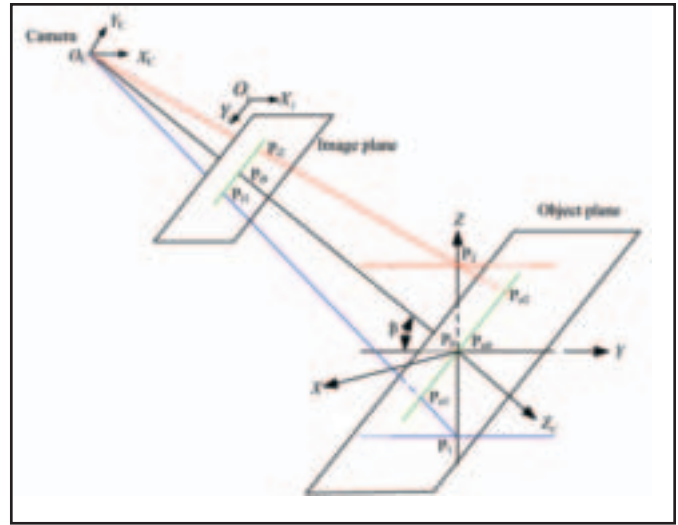


Fig. 2 — The SD measurement principle.

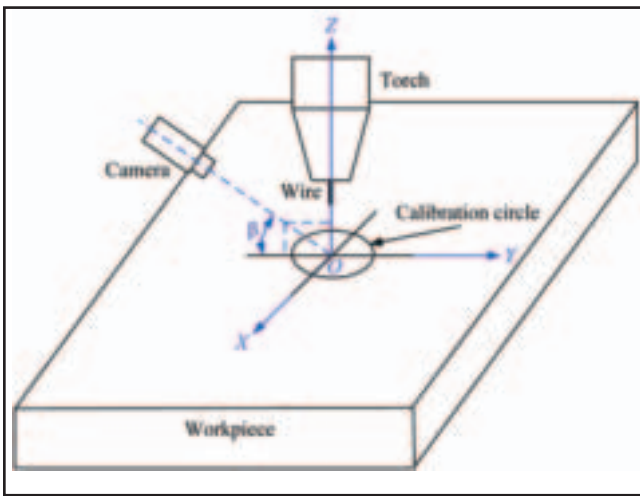


Fig. 3 — Calibration principle.

are capable of controlling the weld penetration only based on observation of the weld pool surface. Hence, methods have been proposed to measure the three-dimensional surface of the weld pool using structured-light and diffuse glass (Ref. 13), structured light and calibrated camera (Ref. 14), specular reflection from the weld pool (Refs. 15, 16), shape from shading (Ref. 17), binocular stereo vision (Ref. 10), and its variant biprism stereo vision (Ref. 18). In another effort, Zhang and Yan measured the average height of the weld pool tail boundary, i.e., depth information from a geometry approximation model in GMAW-P for thin plate (Ref. 19). Unfortunately, these methods are largely based on vision, and the suitability of their use in manufacturing facilities needs to be improved before they may be

actually applied.

This paper explores the development of a simple yet innovative method to effectively derive the depth of the weld pool surface underneath the arc (referred to as the surface depth or SD hereafter) and relate the depth of the weld penetration (penetration depth or PD hereafter) with it. In order to study their relationship, SD is measured directly using machine vision from high-speed cameras. To use signals that are easily measurable to predict PD, the arc voltage is also measured and related to PD.

Vision-Based Measurement Principle

A high-speed camera, OLYMPUS i-SPEED, which is capable of capturing images up to 33,000 frames per second and of directly imaging the weld pool under the presence of the arc, is fixed in the upper side of the weld pool with angle β to view the weld pool as shown in Fig. 1. The welding gun is perpendicular to the workpiece surface. For convenience of discussion, a welding gun coordinate system OXYZ is established as shown in Fig. 1 with the workpiece upper surface as the OXY plane, gun axis as the Z-axis, and weld joint and travel direction as the X-axis.

A vision-based method for SD meas-

urement is shown in Fig. 2. The SD in this paper refers to the maximum weld pool surface depth below the OXY plane, which can be measured using the Z-axis coordinate of the intersection between the Z-axis and the weld pool surface. A pin-hole camera model is employed in this study. The scale in Fig. 2 has been adjusted for better illustration. There are three coordinate systems including the camera coordinate system ($O_C X_C Y_C Z_C$), the image coordinate system ($O_i X_i Y_i$), and welding gun coordinate system. The object plane is parallel to the image plane and forms an angle β with Z-axis. When the weld pool surface rises such that the intersection between the Z-axis and the weld pool surface rises from P_0 to P_2 , the corresponding point in the object plane changes from P_{00} to P_{02} and the corresponding point in the image plane changes from P_{i0} to P_{i2} . The SD can thus be measured as

$$d_s = - | P_2 P_0 | = - | P_{02} P_{00} | / \cos \beta \quad (1)$$

where d_s denotes the SD and a negative/positive d_s indicates a weld pool surface above/below the OXY plane. Similarly, if the weld pool surface lowers, the SD will be

$$d_s = | P_{01} P_{00} | / \cos \beta \quad (2)$$

Define S_c as

$$S_c = | P_{0j} P_{00} | / | P_{ij} P_{i0} | \quad (3)$$

where P_{ij} is the image point of P_j ($j = 1, 2$) in the image plane while P_{0j} is the corresponding point in the object plane. Then,

$$d_s = \pm S_c \times | P_{ij} P_{i0} | / \cos \beta \quad (4)$$

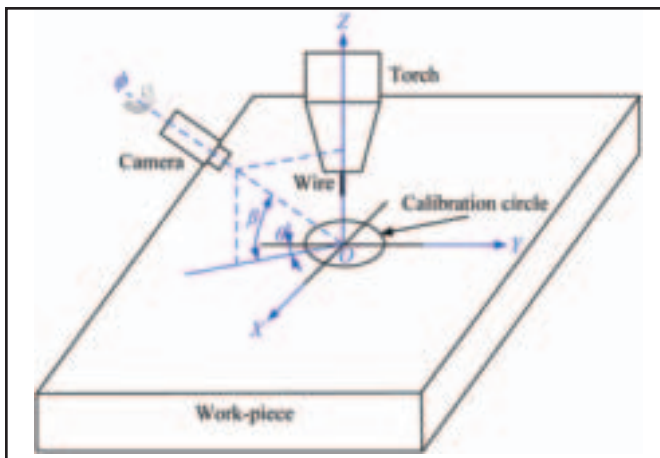


Fig. 4 — Illustration of observation orientation in calibration.

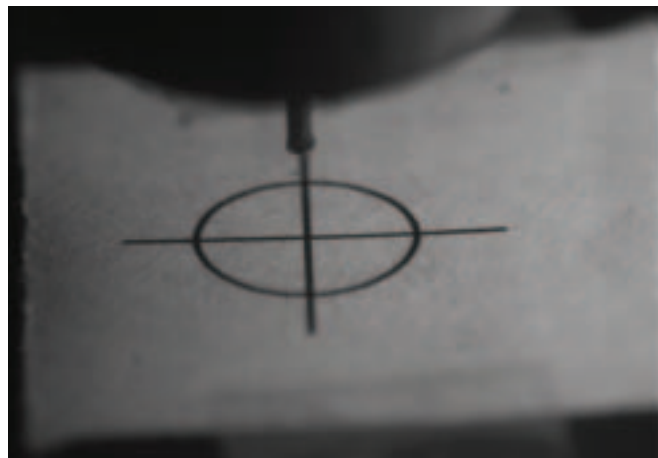


Fig. 5 — Image of the calibration circle with cross.

Hence,

$$d_s = S_c \times (y_{ij} - y_{i0}) / \cos \beta \quad (5)$$

where y_{ij} and y_{i0} are the y-ordinate of P_{ij} ($j = 0, 1, 2$) and the origin, respectively, in the image.

It is apparent that parameters (S_c and β) and position of the origin in the image, i.e., $O(x_{i0}, y_{i0})$, are needed in order to calculate the SD. To this end, a calibration based method was used.

Calibration

A circle has no directionality. Using this characteristic of a circle, a calibration procedure was designed to determine S_c , β , and $O(x_{i0}, y_{i0})$. A calibration circle with a cross was placed right below the wire tip and adhered to the workpiece upper surface as shown in Fig. 3.

Ideally, the optical axis of the camera forms no angle with the OYZ plane; however, there must be a small angle, denoted as θ between them — Fig. 4. In addition, the camera may also have a small rotation angle ϕ as shown in Fig. 4. As the circle has no directionality, the image of the circle will be an ellipse whose long axis is equal to the diameter of the circle and center is the center of the circle. If the parameters of the ellipse, including center position (X_0, Y_0), major semi-axis a , minor semi-axis b , and rotation angle of the ellipse α are obtained from image processing, one can easily determine

$$O = (X_0, Y_0) \quad (6)$$

$$\phi = -\alpha \quad (7)$$

$$S_c = r / a \quad (8)$$

where r is the actual radius of the circle in

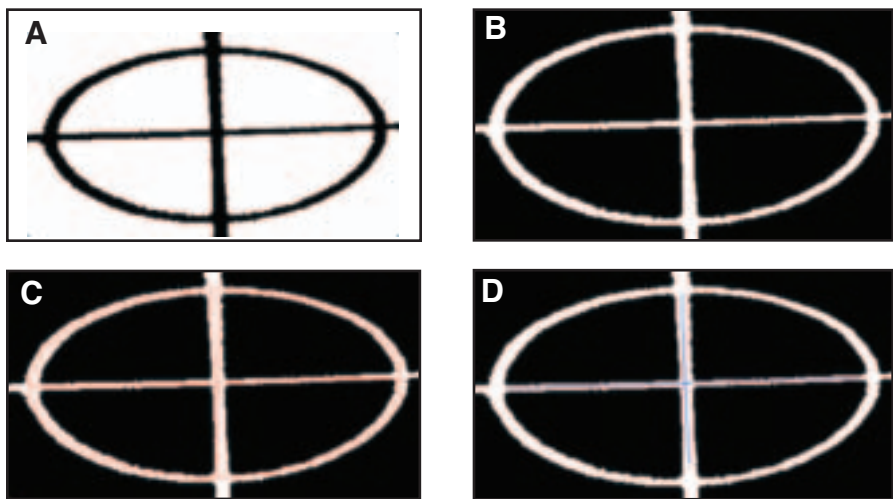


Fig. 6 — Image processing and parameters extraction for calibration. A — Binarization; B — image inverting; C — ellipse fitting; D — lines fitting.

millimeter. Further,

$$\beta = \arcsin(b / a) \quad (9)$$

Also, the slopes and intercepts of the lines k_h, b_h, k_v, b_v can be obtained from image processing. Define $\alpha' = \arctan(k_h)$ and $\varphi = \alpha' - \alpha$, then

$$\theta = \arcsin(\sin \varphi / \sin \beta) \quad (10)$$

The image of the calibration circle is shown in Fig. 5. The area where the loca-

tion of the calibration circle is selected to process, and the image processing results are shown in Fig. 6. The parameters for the ellipse and lines can easily be obtained from the processed image.

Measurement Algorithm Test and Error Analysis

The test principle is shown in Fig. 7. Two metal plates of identical size but different thickness are prepared with identical homocentric round orifices as shown in

Table 1 — Measurement Algorithm Test Result

Calculated Thickness (mm)	Actual Thickness (mm)	Relative Error (%)
6.72	6.35	5.76

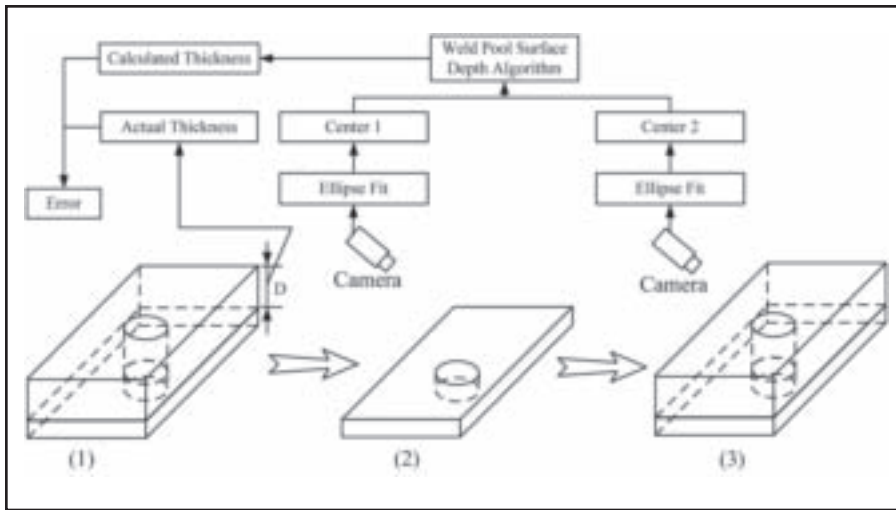


Fig. 7 — Schematic diagram for measurement algorithm test.

Fig. 7(1). After positioning the camera and reference plate, the reference plane, i.e., the top surface of the reference plate, is imaged as shown in Fig. 7(2). Then the

test plate is positioned on top of the reference plate with the two homocentric orifices perfectly aligned and imaged as shown in Fig. 7(3). The two images are

Table 2 — Calculated Parameters List

Parameters	Values
Average welding current (I_a) (A)	192.0
Average welding voltage (U_a) (V)	30.4
Average peak voltage (U_p) (V)	33.6
Average base voltage (U_b) (V)	27.7
Change of welding voltage in every peak period (ΔU_{pi}) (V)	3.83
	2.13
	0.75
	3.33
	1.38
Average change of welding voltage in peak period (ΔU) (V)	2.28
Average SD in peak period (\bar{d}_s) (mm)	-0.33
Change of SD in every peak period (Δd_{si}) (mm)	0.56
	0.52
	1.01
	0.56
	0.38
Average change of SD in peak period (Δd_s) (mm)	0.61
Weld width (W_f) (mm)	6.57
Average weld penetration (d_p) (mm)	2.63

Table 3 — Welding Parameters when $C = 11.4$

No.	TS (m/min)	WFS (m/min)	I_a (A)	I_p (A)	t_p (ms)	I_b (A)	t_b (ms)
11	0.30	3.43	135	300	8	70	20.3
12	0.36	4.11	162	300	8	70	12
13	0.42	4.80	189	300	8	120	12.9
14	0.48	5.49	216	300	8	180	18.7

then processed for the center points of the two ellipses, which can be used to calculate the thickness of the test plate.

In this study, both of the two plates are 100×50 mm, while the thickness is 2.54 mm and 6.35 mm for the reference and test plate, respectively. The diameters of the two identical round orifices are both 6.35 mm. The two original images are in Fig. 8A and B. The ellipse fitting and line fitting results are shown in Fig. 8C and D. The results of the thickness calculation are given in Table 1.

As can be seen in Table 1, there is an error between the actual and calculated thickness. This error can be considered an estimate of the error for the proposed depth calculation algorithm when the weld pool surface changes for 6.35 mm. This error occurs because the algorithm shown in Fig. 2 is actually an approximation of the accurate camera model. As shown in Fig. 9, the error produced by the approximation is $|PP''|$. The error is caused by the approximation used, so it is an inherent error of the depth calculation algorithm. The relative inherent error (δ) is

$$\delta = \frac{(|PP''| - |PP'|)}{|PP'|} = \frac{\cos \eta}{\cos(\beta - \eta)\cos \beta} - 1 \quad (11)$$

It is apparent that, if $\eta \rightarrow \beta$, then $\delta \rightarrow 0$. In the case above, β and η can both be calculated from Equation 9, i.e., $\beta = \arcsin(b/a)$ using a and b from the image of the reference plate and $\eta = \arcsin(b/a)$ using a and b from the image of the test plate, resulting in $\beta = 0.576$ and $\eta = 0.548$. The relative inherent error is thus 2.67%.

There are additional error sources including possible unwanted self rotation of the camera, a small gap between the two plates used in the test, calculation error in calculating the centers of the two ellipses, and so on. The error given in Table 1 is the result of all these sources. However, in actual measurement, the change of the weld pool surface depth is much smaller than 6.35 mm used in the above test such that the error caused by the approximation of camera model is much reduced. Hence, in actual measurement, the error will be much smaller than 5.76% although 5.76% should be considered an acceptable accuracy for weld penetration control.

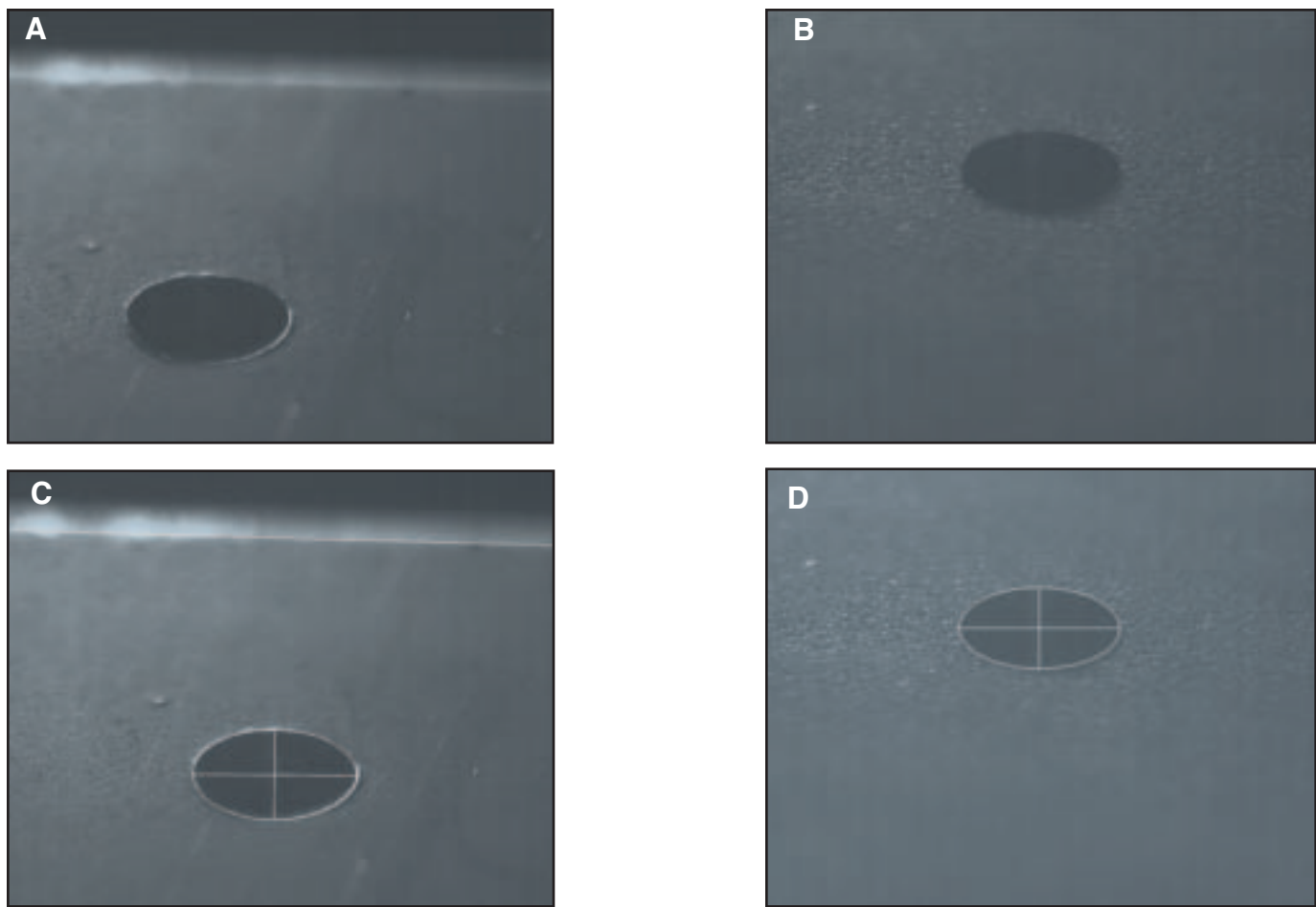


Fig. 8 — Measurement algorithm test images. A — Reference plane; B — test plane; C — fitting result for the reference plane; D — fitting result for the test plane.

Experimental Setup

The experimental setup is shown in Fig. 10. The welding machine runs at constant current (CC) mode and the current is controlled by the target computer through

D/A. The Olympus i-Speed II camera acquires images at 1000 frames per second and stores them in a CF (compact flash) card. The arc voltage and actual current are synchronized with the images as shown in Fig. 11, measured by the target com-

puter and stored in the host computer.

Surface Depth Measurement Experiment

An experiment was conducted to meas-

Table 4 — Welding Parameters when $C = 13.1$

No.	TS (m/min)	WFS (m/min)	I_a (A)	I_p (A)	t_p (ms)	I_b (A)	t_b (ms)
21	0.30	3.94	155	300	8	70	13.6
22	0.36	4.72	186	300	8	70	7.9
23	0.42	5.51	217	300	8	120	6.8
24	0.48	6.30	248	300	8	180	6.1

Table 5 — Welding Parameters when $C = 14.8$

No.	TS (m/min)	WFS (m/min)	I_a (A)	I_p (A)	t_p (ms)	I_b (A)	t_b (ms)
31	0.30	4.45	175	300	8	70	9.5
32	0.36	5.33	210	300	8	70	5.1
33	0.42	6.22	245	300	8	120	3.5
34	0.48	7.11	280	300	8	180	1.6

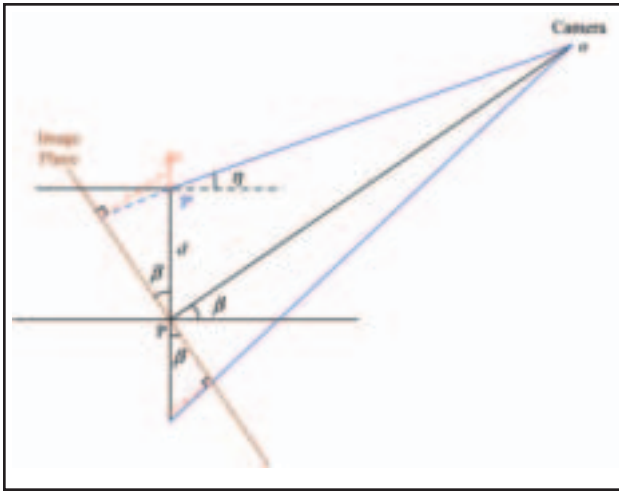


Fig. 9 — Error analysis.

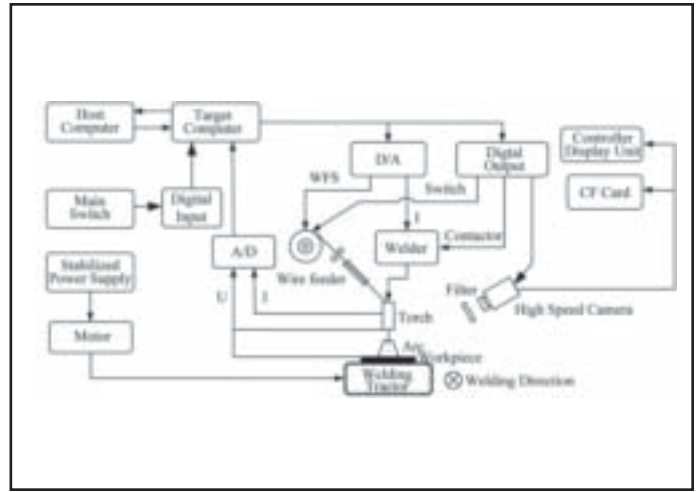


Fig. 10 — Experimental setup.

ure the weld pool surface depth where two 6.3-mm-thick mild steel (C1018) plates of 300 × 25.4 mm were welded in a square-groove butt joint with a 1.5 mm root opening in the flat position. The welding gun stayed stationary and the workpiece traveled with the welding tractor at a constant speed of 0.42 m/min. The contact tip to workpiece distance (CTWD) was 12 mm. The welding wire used was 1.2 mm (0.045 in.) mild steel ER70S-3. The wire feed speed (WFS) was 4.8 m/min (189 in./min). The welding current was pulsed between peak current 300 A and base current 120 A. The pulse period was 20.9 ms and the duty ratio was 38.3%. The shielding gas was pure argon and the flow rate was 18.9 L/min (40 ft³/h).

A weld pool image obtained by the high-speed camera is shown in Fig. 12. The center of the weld pool surface is defined as the center of the elliptical weld pool and is marked by the red asterisk as shown in Fig. 12.

Using the algorithm developed earlier, SD in the peak current period can be calculated and synchronized with the welding current/voltage waveforms as shown in Fig. 13. The average SD can also be calculated

$$\bar{d}_s = (\sum d_s) / k \quad (12)$$

where k is number of the SD measurements used. Because the weld pool surface is fluctuating due to the metal transfer, measurement averaging is necessary.

Denote any SD measurements in the i th peak period as a d_{si} . The change of the SD in the i th peak period is

$$\Delta d_{si} = \max(d_{si}) - \min(d_{si}) \quad (13)$$

The average change in different peak periods is

$$\Delta d_s = \left(\sum_{i=1}^n \Delta d_{si} \right) / n \quad (14)$$

where n is the number of peak current periods of concern.

All above measurements from the experiment are listed in Table 2 together with other parameters/variables such as the change of the voltage in the i th peak period (ΔU_{pi}) and the average change of voltage in different peak periods (ΔU), which will be discussed later, the weld width (W_f), and the average of the weld penetration (d_p) that was measured through the gap from the backside.

Modeling

Experiment Design

In analyzing the GMAW process, not only the welding current/voltage, but also the wire feed speed and welding travel speed (TS) affect SD and PD. When the wire feed speed increases or the travel speed decreases, the PD increases. To concentrate the study on the effect of welding

Table 6 — Welding Parameters when $C = 16.5$

No.	TS (m/min)	WFS (m/min)	I_a (A)	I_p (A)	t_p (ms)	I_b (A)	t_b (ms)
41	0.30	4.95	195	300	8	70	6.7
42	0.36	5.94	234	300	8	70	3.2
43	0.42	6.93	273	300	8	120	1.4
44	0.48	7.92	312	324	8	300	8

Table 7 — Welding Parameters when $C = 18.2$

No.	TS (m/min)	WFS (m/min)	I_a (A)	I_p (A)	t_p (ms)	I_b (A)	t_b (ms)
51	0.30	5.46	215	300	8	70	4.7
52	0.36	6.55	258	300	8	70	1.8
53	0.42	7.65	301	302	8	300	8
54	0.48	8.74	344	388	8	300	8

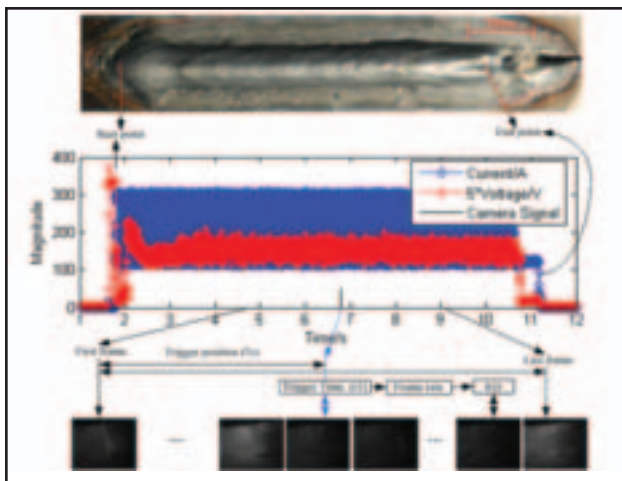


Fig. 11 — Synchronization of measurements.



Fig. 12 — Weld pool image and weld pool surface center.

current/voltage, the metal deposition can first be controlled at a constant C .

$$WFS / TS = C \quad (15)$$

Then C can be changed in order to study the effect from the metal deposition on the SD and PD.

When designing an experiment, the travel speed is first specified at a value from 0.3 m/min to 0.48 m/min, typical for GMAW. Then the wire feed speed is determined based on C used. The average welding current has been determined approximately by the wire feed speed and is used as a constraint in the current pulse waveform design. Also, to facilitate the possibility where the arc voltage is easily measurable in manufacturing facilities with SD, the effect of the current on the

relationship between arc length and arc voltage needs to be overcome. Hence, the peak current and its period are set constants and the base current and its period are determined based on the average current. In this study, 300 A and 8 ms were used as the peak current amplitude and period. The welding parameters designed are shown in Tables 3–7 for five series of experiments with five different C .

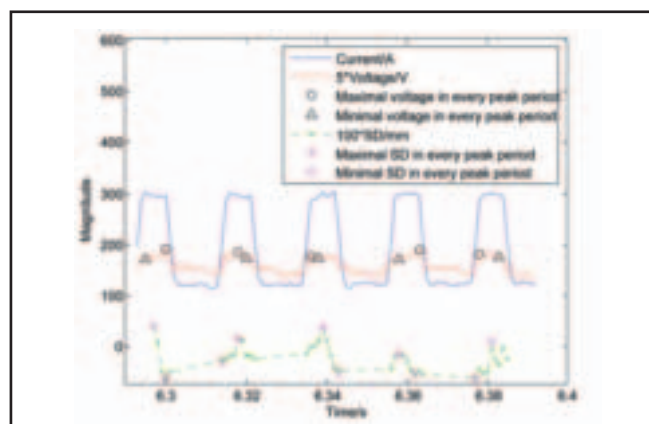


Fig. 13 — Welding current/voltage and SD. Current and voltage signals shown are averages of the measurements for the present and last previous point.

Table 8 — Experimental Results for Modeling

No.	C	I_a (A)	Welding Voltage (V)			\bar{d}_s (mm)	Δd_s (mm)	ΔU (V)	W_f (mm)	d_p (mm)
			U_a	U_p	U_b					
11	11.4	136.8	26.4	31.3	22.4	0.45	0.84	3.59	6.38	1.62
12	11.4	158.6	28.2	32.4	24.4	0.28	0.72	2.46	6.70	2.51
13	11.4	192.0	30.4	33.6	27.7	-0.33	0.61	2.28	6.57	2.63
14	11.4	218.1	31.3	33.8	29.7	-0.16	0.45	1.93	5.61	2.64
21	13.1	154.1	27.9	31.9	23.8	0.33	0.68	3.19	7.85	1.93
22	13.1	182.1	30.1	34.1	25.7	0.16	0.49	1.65	6.87	2.58
23	13.1	212.1	30.4	33.4	27.1	-0.17	0.44	1.16	8.90	3.01
24	13.1	246.4	32.7	34.4	30.6	-0.31	0.41	1.05	6.59	3.23
31	14.8	176.4	30.1	34.1	26.4	0.31	0.57	2.23	8.17	2.45
32	14.8	211.4	31.7	35.2	27.6	0.05	0.43	1.28	8.81	2.83
33	14.8	243.6	32.0	34.2	28.8	0.04	0.40	0.99	11.13	3.27
34	14.8	275.9	34.8	35.9	33.4	0.69	0.38	0.76	7.88	3.31
41	16.5	192.4	30.7	34.3	26.6	0.15	0.42	1.82	8.66	2.60
42	16.5	230.1	32.5	34.8	28.8	0.02	0.37	1.22	10.83	3.27
43	16.5	271.7	34.5	35.5	32.4	0.30	0.33	0.81	8.98	3.33
44	16.5	308.2	35.6	36.2	35.0	1.00	0.17	0.74	8.55	3.45
51	18.2	211.1	31.5	34.6	27.6	-0.43	0.39	1.73	11.54	2.93
52	18.2	254.8	33.4	34.9	30.2	-0.01	0.30	1.06	9.17	3.74
53	18.2	298.3	35.1	35.6	34.5	0.33	0.24	0.79	14.69	4.09
54	18.2	334.9	37.1	38.4	35.7	1.05	0.16	0.94	7.41	4.35

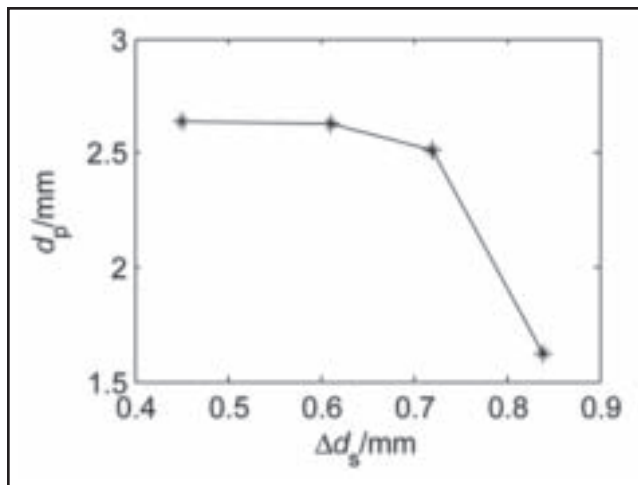


Fig. 14 — Relationship between Δd_s and weld penetration when $C = 11.4$.

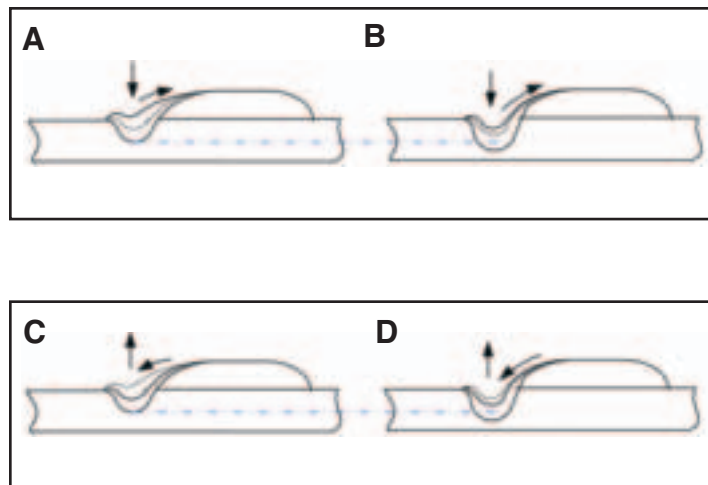


Fig. 15 — Different penetrations Δd_s . A — Peak period; B — peak period in deeper penetration; C — base period; D — base period in deeper penetration.

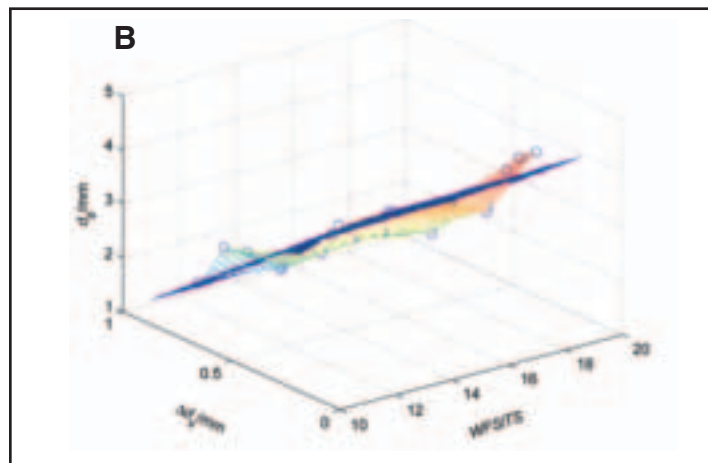
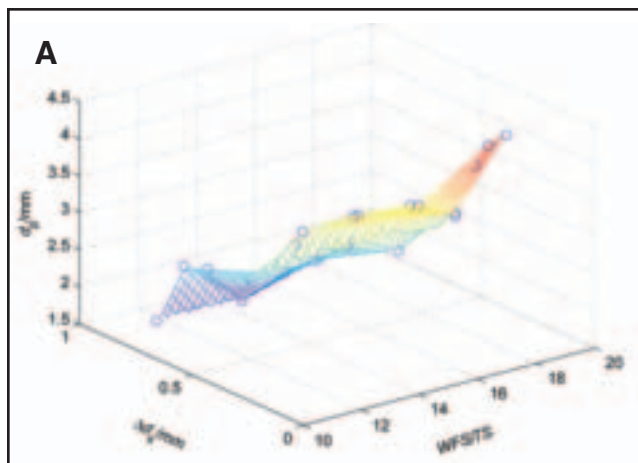


Fig. 16 — Modeling. A — Nonparametric graphic model; B — plane model.

Results and Discussion

Using the welding parameters in Tables 3–7, five series of experiments were conducted and the results are given in Table 8.

As can be seen from Table 8, when WFS/TS is constant, with the increase in the average current, average change of SD in peak period decreases, while PD increases. Take $C = 11.4$ as an example; the relationship between the average change of SD in peak periods and the PD is shown in Fig. 14.

In analyzing the GMAW-P process, when the impact of droplets is not considered, the front of the weld pool head is pressed down by the arc and the molten metal flows upward to the tail of the weld pool during the peak period as shown in Fig. 15A. In the base period, the molten metal flows back to the front due to the

decrease of the arc pressure and the weld pool surface rises as shown in Fig. 15C. When the metal deposition is unchanged, the SD and arc length will increase if the PD increases as shown in Fig. 15B.

From another point of view, if the weld penetration increases, it must be caused either by an increase in the base current or a decrease in the base period because the peak current amperage and period are kept constant. Since the arc pressure in the base period will increase if the base current increases or the molten metal will have less time to flow back if the base period time decreases, a deeper penetration will result in that less metal flows back by the end of the base period as shown in Fig. 15D. Further, it is likely that the weld pool surface will be pushed to the same level due to the unchanged peak current amperage and period. Hence, the change of SD during the

peak period would tend to reduce as was observed from Table 8 and Fig. 14.

When the droplet is taken into consideration, the change of SD in peak current period should change. However, the peak current amperage and period are maintained unchanged and do not change with experiments. The effect of the impact of the droplet on the change of SD should be considered unchanged with experiment. Hence, the droplet should not change how the average change of SD in peak period is related to the weld penetration when the WFS/TS is constant in the GMAW-P process.

Taking WFS/TS as a factor into account, the weld penetration is the function of Δd_s and WFS/TS

$$d_p = f(\Delta d_s, WFS/TS) \quad (16)$$

The interpolation of data can give a non-

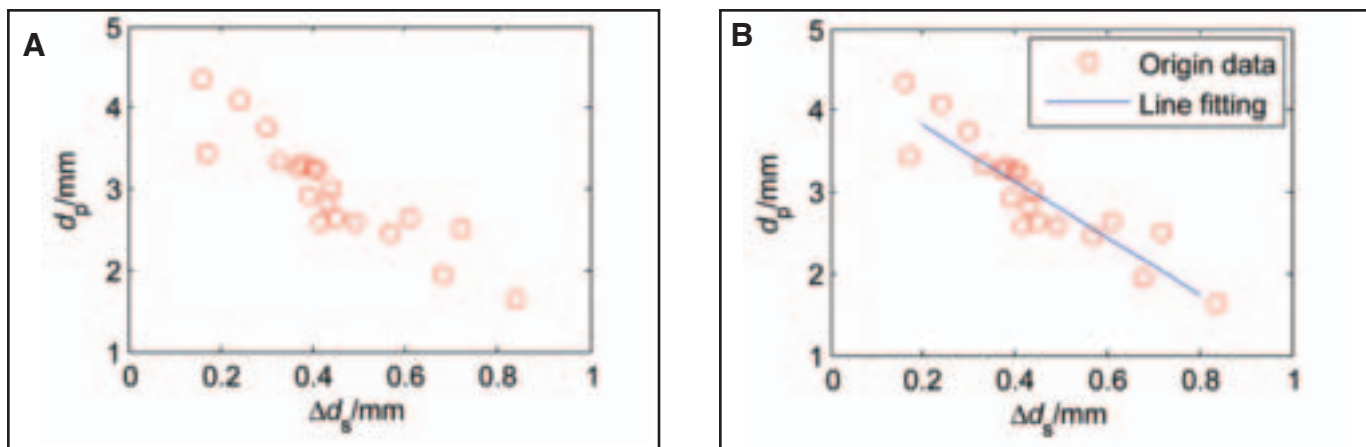


Fig. 17 — Modeling without WFS/TS. A — Δd_s vs. penetration; B — line fitting.

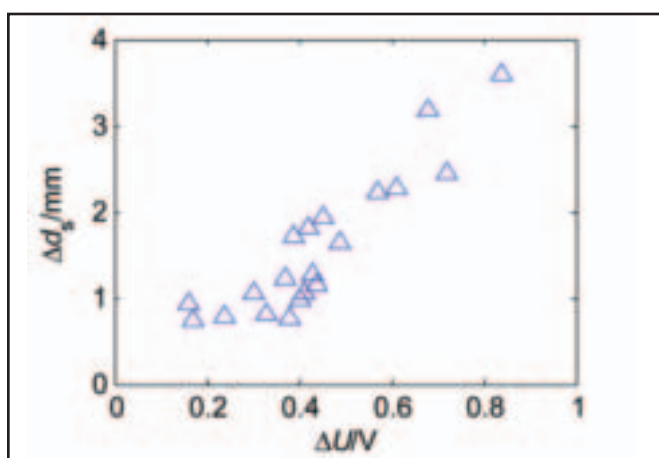


Fig. 18 — ΔU vs. Δd_s .

parametric graphic model for the relationship (Equation 16) as shown in Fig. 16A. As can be seen, the surface in Fig. 16A is close to a plane. Hence, a plane model can be fitted

$$d_p = -3.34 \times \Delta d_s + 0.01 \times WFS/TS + 4.31 \quad (17)$$

with a standard deviation of 0.27 mm. The fitting plane is shown in Fig. 16B with the interpolation of data. This linear plane model has sufficient accuracies for weld penetration control in the GMAW-P process.

Analysis of Model 17 shows that the second term with WFS/TS has little contribution to the weld penetration. Hence, it is possible that the model can be simplified without consideration of WFS/TS . Using a straight line to fit, the result is shown in Fig. 17B and the resultant model is

$$d_p = -3.45 \times \Delta d_s + 4.51 \quad (18)$$

with a standard deviation of 0.27 mm. The

accuracy is as good as the plane model. Hence, the depth of the weld penetration can be predicted, with an acceptable accuracy, by the change of the weld pool surface depth during the peak current period.

Modeling for Practical Application

While the result that the depth of the weld penetration can be predicted by the change of the weld pool surface depth

during the peak current period is fundamental, its direct application in penetration control in manufacturing facilities could be complex if the weld pool surface depth is measured using a machine vision method. To find a method to monitor the weld penetration using signals that are easily measurable in manufacturing plants, a possible relationship between the change in weld pool surface depth and a change in arc voltage is thought because 1) a surface change will cause the arc length to change, and 2) a change in the arc length can be measured from the arc voltage. In the peak current period, the current is constant and the arc voltage is only determining the arc length. Hence, it is possible that the change of the arc voltage in the peak current period may reflect a change in weld pool surface depth.

For quantitative studies, let's similarly define the change of the voltage in the i th peak period as

$$\Delta U_{pi} = \max(U_{pi}) - \min(U_{pi}) \quad (19)$$

and the average change in different peak periods as

$$\Delta U = \left(\sum_{i=1}^n \Delta U_{pi} \right) / n \quad (20)$$

From the experimental data as given in Table 8, Fig. 18 is obtained. It is apparent that ΔU and Δd_s are highly correlated as expected. A model can be easily established to correlate them.

Using ΔU to replace Δd_s , the following model is fitted:

$$d_p = -0.56 \times \Delta U + 0.08 \times WFS/TS + 2.69 \quad (21)$$

The standard deviation is 0.27 mm, and it is the same as for Model 17. Further, the following model can be fitted from the experimental data in Table 8

$$d_p = -0.71 \times \Delta U + 4.12 \quad (22)$$

Its standard deviation is 0.31 mm, slightly higher than that using both ΔU and $C = WFS/TS$. For weld penetration control, this model can be considered as effective as Model 21. Because Model 22 only uses voltage signals, it is suitable for practical applications in manufacturing facilities.

Conclusions

- The weld pool surface indeed contains sufficient information to determine the depth of the weld penetration as expected during GMAW-P.
- The depth of the weld penetration can be determined with adequate accuracy from the change of the weld pool surface depth during the peak current period.
- The depth of the weld penetration can also be determined with adequate accuracy from the change in arc voltage during the peak current period.

• Because the arc voltage is easily measurable in manufacturing plants, the relationship confirmed in this study between the depth of the weld penetration and the change of the arc voltage during the peak current period provides a simple yet suitable method to monitor the weld penetration for manufacturing applications.

Acknowledgment

This work was funded by the National Science Foundation under grant CMMI-0726123 entitled Measurement and Control of Dynamic Weld Pool Surface in Gas Metal Arc Welding. This work was performed at the Welding Research Laboratory at the University of Kentucky.

References

1. Kim, Y. S., and Eagar, T. W. 1993. Analysis of metal transfer in gas metal arc welding. *Welding Journal* 72: 269-s to 278-s.
2. Esser, W. G., and van Gompel, M. R. M. 1984. Arc control with pulsed GMA welding. *Welding Journal* 63: 26-s to 32-s.
3. Ueguri, S., Hara, H., and Komura, H. 1985. Study of metal transfer in pulsed GMA welding. *Welding Journal* 64: 242-s to 250-s.
4. Allum, C. J. 1985. Welding technology data: pulsed MIG welding. *Welding and Metal*

Fabrication 53: 24–30.

5. Kovacevic, R., Zhang, Y. M., and Ruan, S. 1995. Sensing and control of weld pool geometry for automated GTA welding. *ASME Journal of Engineering for Industry* 117(2): 210–222.
6. Chin, B. A., Madsen, N. H., and Goodling, J. S. 1983. Infrared thermography for sensing the arc welding process. *Welding Journal* 62: 227-s to 234-s.
7. Madigan, R. B., Renwich, R. J., Farson, D. F., and et al. 1986. Computer-based control of full-penetration TIG welding using pool oscillation sensing. *Proceedings of First International Conference on Computer Technology in Welding*, The Welding Institute, London.
8. Xiao, Y. H. 1992. Weld pool oscillation during gas tungsten arc welding. Ph.D. dissertation. Delft, The Netherlands, Delft University of Technology.
9. Wang, Q. L. 1991. Real-time full-penetration control with arc sensor in the TIG welding of Al alloy. *Proceedings of the International Conference on Joining/Welding 2000*, IIW, the Netherlands.
10. Mnich, C., Al-Bayat, F., Debrunner, C., and et al. 2004. In situ weld pool measurement using stereovision. *ASME, Proceedings 2004, Japan – USA Symposium on Flexible Automation*, Denver, Colorado.
11. Siores, E. 1988. Development of a real-time ultrasonic sensing system for automated and robotic welding. PhD dissertation. West London, UK, Brunel University.
12. Groenwald, R. A., Mathieson, T. A., Kedzior, C. T., et al. 1979. Acoustic emission weld

- monitor system — data acquisition and investigation. *US Army Tank-Automotive Research and Development Command Report ADA085-518*.
13. Kovacevic, R., and Zhang, Y. M. 1997. Real-time image processing for monitoring of free weld pool surface. *ASME Journal of Manufacturing Science and Engineering* 119(2): 161–169.
 14. Saeed, G., and Zhang, Y. M. 2007. Weld pool surface depth measurement using calibrated camera and structured-light. *Measurement Science & Technology* 18: 2570–2578.
 15. Song, H. S., and Zhang, Y. M. 2007. Three-dimensional reconstruction of specular surface for gas tungsten arc weld pool. *Measurement Science & Technology* 18: 3751–3767.
 16. Song, H. S., and Zhang, Y. M. 2008. Measurement and analysis of three-dimensional specular gas tungsten arc weld pool surface. *Welding Journal* 87(4): 85-s to 95-s.
 17. Zhao, D. B. 2000. Dynamic intelligent control for weld pool shape during pulsed GTAW with wire filler based on three-dimension visual sensing. Ph.D. dissertation. Harbin, China, Harbin Institute of Technology (in Chinese).
 18. Yoo, C. D., and Lee, J. 3D measurement of weld pool using biprism stereo vision sensor. <http://joining1.kaist.ac.kr/research/vision.htm>, Seoul National University.
 19. Zhang, G. J., Yan, Z. H., and Wu, L. 2006. Reconstructing a three-dimensional P-GMAW weld pool shape from a two-dimensional visual image. *Measurement Science and Technology* 17(7): 1877 to 1882.

Good News:

I'm glad to announce that peer review of research papers is now managed through an online system using Editorial Manager software. Papers can be submitted into the system directly from the *Welding Journal* page on the AWS Web site by clicking on "submit papers." You can also access the new site directly at www.editorialmanager.com/wj/. Follow the instructions to register or login, and make sure your information is up to date. This online system will streamline the review process, and make it easier for authors to submit papers and track their progress. If you have any questions or encounter problems, please click on "help" or "contact us" in the main navigation bar.

Best Regards,

Andrew Cullison
Publisher
Welding Journal